Journal of Nuclear Materials 580 (2023) 154410

Contents lists available at ScienceDirect

Journal of Nuclear Materials

journal homepage: www.elsevier.com/locate/jnucmat

Detecting irradiation-induced strain localisation on the microstructural level by means of high-resolution digital image correlation

D. Lunt[a,b,*], R. Thomas[a], D. Bowden[a,b], M.T.P. Rigby-Bell[a,b], S. de Moraes Shubeita[c], C. Andrews[c], T. Lapauw[d], J. Vleugels[d], J. Quinta da Fonseca[a], K. Lambrinou[e], P. Frankel[a]

[a] Department of Materials, University of Manchester, Oxford Road, United Kingdom of Great Britain and Northern Ireland, Manchester, UK
[b] UKAEA, Culham Science Centre, United Kingdom of Great Britain and Northern Ireland, Abingdon OX143DB, UK
[c] Dalton Cumbrian Facility, University of Manchester, United Kingdom of Great Britain and Northern Ireland, Westlake's Science Park, UK
[d] Department of Materials Engineering, KU Leuven, Kasteelpark Arenberg 44, Leuven 3001, Belgium
[e] School of Computing and Engineering, University of Huddersfield, Queensgate, United Kingdom of Great Britain and Northern Ireland, Huddersfield HD13DH, UK

ARTICLE INFO

Article history:
Received 26 January 2023
Revised 22 March 2023
Accepted 23 March 2023
Available online 24 March 2023

Keywords:
Irradiation growth
High-resolution digital image correlation (HRDIC)
Zirconium alloys
MAX phases
Microcracking

ABSTRACT

Materials subjected to irradiation damage often undergo local microstructural changes that can affect their expected performance. To investigate such changes, this work proposes a novel approach to detect strain localisation caused by irradiation-induced damage in nuclear materials on the microstructural level, considering a statistically relevant number of grains. This approach determines local strains using high-resolution digital image correlation (HRDIC) and compares them with the underlying material microstructure. Sets of images captured before and after irradiation are compared to generate full-field displacement maps that can then be differentiated to yield high-resolution strain maps. These strain maps can subsequently be used to understand the effects of irradiation-induced dimensional change and cracking on the microscale. Here, the methodology and challenges involved in combining scanning electron microscopy (SEM) with HRDIC to generate strain maps associated with radiation-induced damage are presented. Furthermore, this work demonstrates the capabilities of this methodology by analysing three different materials subjected to proton irradiation: a zircaloy-4 (Zry-4) metal irradiated to 1 & 2 dpa, and two ceramics based on MAX phase compounds, i.e., the Nb_4AlC_3 ternary compound and a novel $(Ta,Ti)_3AlC_2$ solid solution, both irradiated to ~0.1 dpa. These results demonstrated that all materials show measurable expansion, and the very high strains seen in the MAX phase ceramics can be easily attributed to their microstructure. Grain-to-grain variability was observed in Zry-4 with a macroscopic expansion along the rolling direction that increased with irradiation damage dose, the Nb_4AlC_3 ceramic showed significant expansion within individual grains, leading to intergranular cracking, while the less phase-pure $(Ta,Ti)_3AlC_2$ ceramic exhibited very high strains at phase boundaries, with limited expansion in the binary carbide phases. This ability to measure irradiation-induced dimensional changes at the microstructural scale is important for designing microstructures that are structurally resilient during irradiation.

1. Introduction

All materials proposed for nuclear applications require both chemical and structural stability at the expected operating temperatures as well as resistance to irradiation damage. Furthermore, materials proposed for Gen-IV fission reactor applications must withstand the system-specific nominal operating conditions for prolonged periods of time, combining resistance to high-temperature transients with exceptional radiation tolerance (up to 200 dpa). Therefore, it is imperative to carry out a detailed characterisation of all candidate materials for such applications at both the microscale level, as often the local strains on a sub-grain scale are critical to failure prediction, and the macroscale level to identify conditions that may lead to in-service material failure.

Zirconium-based alloys are extensively used by the nuclear industry as fuel cladding and channel materials for light water reactors (LWRs), due to the combination of a small thermal neutron cross-section with good mechanical properties and satisfactory hydrothermal corrosion resistance [1]. A particularly important phenomenon for zirconium alloy fuel cladding materials

* Corresponding author.
E-mail address: dave.lunt@ukaea.uk (D. Lunt).

https://doi.org/10.1016/j.jnucmat.2023.154410

is irradiation-induced growth, i.e., dimensional changes caused by the accumulation of irradiation-induced defects without any externally applied load [2,3]. Dimensional changes due to irradiation growth of components situated in the reactor core, such as fuel cladding tubes, may lead to in-service operational issues [2], such as incomplete rod insertion and channel bowing.

The MAX phases are a class of materials considered for the fabrication of anticorrosion coatings on fuel cladding tubes in different fission reactor systems, which are nanolayered ternary carbides or nitrides characterised by a remarkable combination of properties, some characteristic of metals and some characteristic of ceramics [4]. The MAX phases are described by the $M_{n+1}AX_n$ general stoichiometry, where M is an early transition metal (e.g., Ti, Zr, Nb, Cr, Ta), A is an element predominantly from groups 13–16 in the periodic table (typically, Al or Si), X is C or N, and $n = 1$, 2, or 3 [5]. Prior experiments have shown that different MAX phases respond differently to irradiation [6–10] and corrosion [11–14], depending on their exact stoichiometry. For example, the extensively studied Ti-based MAX phases exhibit good radiation tolerance provided that the irradiation temperature is >700 °C [6,7], but suffer from anisotropic swelling, decomposition into the respective binary carbide (TiC), and microcracking at lower temperatures [6,8]. Bowden et al. [15] observed a similar behavior in Zr_3AlC_2 that undergoes decomposition around 400 °C, and in Nb_4AlC_3 that exhibits severe intergranular microcracking at 350 °C. Overall, MAX phase-based ceramics that were not optimized for nuclear applications have so far demonstrated a limited capability for dynamic recovery of radiation-induced defects at temperatures ≤400 °C. Both zirconium and MAX phase compounds undergo dimensional changes on the grain level due to irradiation and, thus, this local incompatibility is an issue and understanding the impact of this is critical to predicting component lifetime.

Analytical techniques that have been used extensively to investigate radiation-induced effects in nuclear materials are transmission electron microscopy (TEM) and X-ray diffraction (XRD), where TEM is typically utilised for dislocation analysis on the nanoscale over a limited number of grains, whilst XRD provides data pertaining to irradiation-induced changes across many grains. However, very little research has tried to monitor the relative response of a material to proton irradiation on a microstructural scale, especially for a statistically relevant number of grains. For this reason, being able to determine the local changes due to irradiation across multiple grains, using a single technique, would be very advantageous. The objective of this work is to develop a new analytical technique capable of detecting and quantifying irradiation-induced changes on the microscale. One such technique is digital image correlation (DIC) that is used to study local changes on the surface of a material; the general principle of DIC is to track distinct features in an image of an altered state with respect to the reference image of the original state [16–18]. The spatial resolution required to resolve small changes any material is likely to undergo during irradiation to low damage levels (<1 dpa) is possible due to recent developments in sample patterning [19–21] as well as image acquisition and processing [22]. This is referred to as high-resolution digital image correlation (HRDIC) and was primarily developed to study plastic deformation in metals [23–26]. In this work, however, it is specifically adapted to detect proton irradiation-induced changes in different nuclear materials (metals & ceramics).

To investigate whether it is possible to measure the changes materials undergo during proton irradiation using HRDIC, the surfaces of a zircaloy (i.e., Zry-4) and two MAX phase ceramics (i.e., Nb_4AlC_3 and $(Ta,Ti)_3AlC_2$) were pre-applied with a gold-remodelled pattern [27–29], which was then imaged using a field emission gun scanning electron microscope (FEG-SEM). After proton irradiation, the remodelled pattern was re-imaged to enable strain mapping, employing HRDIC to measure irradiation-induced strains and, subsequently, the response was correlated directly with the material microstructure captured by orientation mapping.

2. Experimental methodology

2.1. Materials

Two materials with different expected irradiation responses were used for the main comparison in this study: laboratory-grade Nb_4AlC_3 supplied by KU Leuven, and recrystallised Zircaloy-4 (Zry-4; Zr-1.5Sn-0.2Fe-0.1Cr, in wt.%) supplied by Rolls-Royce Plc. The effect of speckle patterning at a lower temperature than the experimental irradiation temperature was also assessed on a novel $(Ta,Ti)_3AlC_2$ solid solution with the $(Ta_{0.25},Ti_{0.75})_3Al_{0.77}C_2$ stoichiometry. The novel $(Ta,Ti)_3AlC_2$ MAX phase solid solution was developed at Drexel University for specific fusion applications [30]. The MAX phase-based ceramics were cut into matchsticks with dimensions of 2 × 20 × 2 mm and the Zry-4 metallic samples were machined into tensile specimens with gauge dimensions of 3 × 26 × 1 mm, using electro-discharge machining (EDM). The specimen surface to be proton irradiated was polished to a mirror finish to provide a deformation-free surface, whilst all other specimen surfaces were slightly ground to ensure that all surfaces were conductive during irradiation. Grain orientation mapping was carried out at an accelerating voltage of 20 kV on a FEI Sirion SEM equipped with an Oxford Instruments AZtec electron backscatter diffraction (EBSD) system with a Nordlys II detector. The EBSD maps were analysed with the HKL Channel 5^{TM} software.

2.2. Proton irradiation

Proton irradiation is commonly used as a surrogate for neutron irradiation [31–37], as the comparable sample activation is minimal and protons have a higher displacement rate, meaning a particular damage level can be reached in a fraction of the neutron irradiation time. Proton (H^+) irradiation was carried out at the Dalton Cumbrian Facility (DCF). Samples were either placed across an indium-well or silver pasted on the backing plate directly on top of the heater, and were then secured using both steel and tantalum shims. A detailed schematic of the experimental setup is provided in [15]. Both Zry-4 and Nb_4AlC_3 were irradiated with 2 MeV protons at 350 °C (Table 1) to simulate LWR nominal operation conditions. MAX phase-based ceramics have shown irradiation-induced microcracking in the 300–400 °C range [6,38,39], an undesirable effect. Irradiating at 350 °C was expected to validate the proposed analysis method, due to severe material damage. In the case of the $(Ta,Ti)_3AlC_2$ MAX phase solid solution sample, the irradiation temperature was increased to 650 °C to simulate a mild design-basis transient for LWRs or nominal operation for select applications in Gen-IV fission systems and/or fusion, for example, as armour or

Table 1
Summary of the sputtering and remodelling conditions for each proton-irradiated sample.

Material	Sputter coater	Sputtering conditions	Remodelling vapour	Remodelling conditions	Pattern stabilisation conditions	Irrad. T (°C)
Zry-4	Edwards S150B	3 min at 40 mA	Argon-styrene [27]	200 °C for 36 h	350 °C for 5 days	350
Nb_4AlC_3	Edwards S150B	5.5 min at 40 mA	Water vapour [41]	285 °C for 3 h	350 °C for 12 h	350
$(Ta,Ti)_3AlC_2$	Edwards S150B	5.5 min at 40 mA	Water vapour [41]	285 °C for 3 h	600 °C for 9 h	650

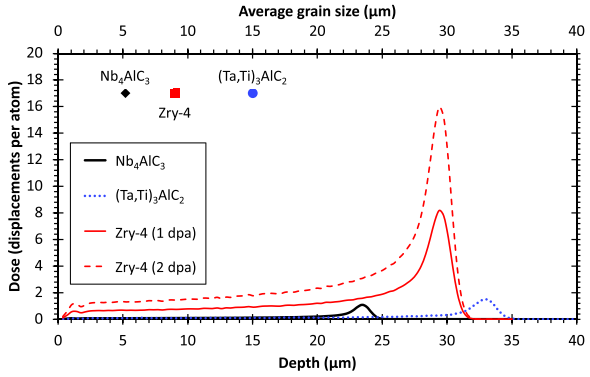

Fig. 1. SRIM profiles for Nb_4AlC_3, $(Ta,Ti)_3AlC_2$ and Zry-4 calculated for 2 MeV H^+ ions at a dose rate of $\sim 6 \times 10^{-6}$ dpa/s, while the average grain sizes of all materials are indicated by dedicated markers next to the secondary *x*-axis.

shielding (either first wall or blanket shield) (Table 1). Dose profiles for Nb_4AlC_3, $(Ta,Ti)_3AlC_2$ and Zry-4, as shown in Fig. 1 where the average grain size is indicated to several grains through the irradiated region, were simulated using the Stopping Range of Ions in Matter (SRIM) 2013 software package. The quick Kinchin-Pease calculation was applied to simulate the collision of 100,000 H^+ ions onto the sample surface. Standard displacement threshold energy values were used for the SRIM calculations, i.e., 25 eV for Nb & Al, 28 eV for C, 30 eV for Ti, 40 eV for Zr and 90 eV for Ta [40]. For 2 MeV H^+, the Bragg peak of maximum damage in Nb_4AlC_3 (theoretical density = 7.04 g/cm^3), $(Ta,Ti)_3AlC_2$ (theoretical density $\approx$ 6.12 g/cm^3) and Zry-4 (theoretical density = 6.55 g/cm^3) is situated at 23.5, 28.5, and 33.2 μm, respectively, beneath the irradiated specimen surface. The irradiated areas in all samples were in the range of 0.5 to 1.0 cm^2. The irradiation parameters were adjusted to provide a constant dose rate of $\sim 6 \times 10^{-6}$ dpa/s throughout, as simulated by SRIM, resulting in damage doses of -0.1 dpa in the Nb_4AlC_3 and $(Ta,Ti)_3AlC_2$ MAX phase samples and 1 & 2 dpa in the two Zry-4 samples, respectively. The quoted dpa values and dose rates were taken at 60% of the depth of the Bragg peak maximum, where the predicted damage profiles were relatively flat. In each material, there is at least one grain through the depth of the plateau region, such that the surface response captured by the high-resolution strain measurement will be highly representative of the irradiation effects. This assumption has been made as no strain patterning was observed when the materials were subjected to temperature without irradiation. It should also be noted that the non-uniformity of the damage profile is not expected to have a significant impact on the surface response, as the Bragg peak itself corresponds to a small fraction of the overall depth of irradiation and it is situated furthest from the sample surface.

2.3. Methodology to detect irradiation-induced strains

2.3.1. Speckle patterning

HRDIC is used to determine local strains caused by proton irradiation, where the same features are tracked before and after irradiation and the corresponding displacements are differentiated to calculate the different strain components [16], enabling the changes to be fully quantified. To perform HRDIC, a uniform pattern must be applied on the surface of the sample prior to proton irradiation. Here, the pattern was applied by the gold remodeling technique, using water vapor remodeling [41] for the Nb_4AlC_3 and $(Ta,Ti)_3AlC_2$ MAX phase ceramics and styrene remodeling [27] for the Zry-4. Styrene remodeling was used for the Zry-4 sample due to the oxidation susceptibility of this material in a water vapour environment. It should be noted that the Nb_4AlC_3 and Zry-4 samples were initially remodeled at 200 and 285 °C, respectively, and then further stabilised near the irradiation temperature (350 °C) for 3–4 times longer than for standard deformation studies [42,43] to ensure that the pattern is stable and will not develop during proton irradiation. For these two materials, the further stabilisation treatment was performed in the same remodelling environment as in the initial stabilisation step. To assess the impact of failing to match the targeted experimental temperature (e.g., faulty thermocouple used in the remodeling/furnace treatment, poor temperature calibration during irradiation, increase in beam current during the experiment resulting in a rise of the irradiation temperature),

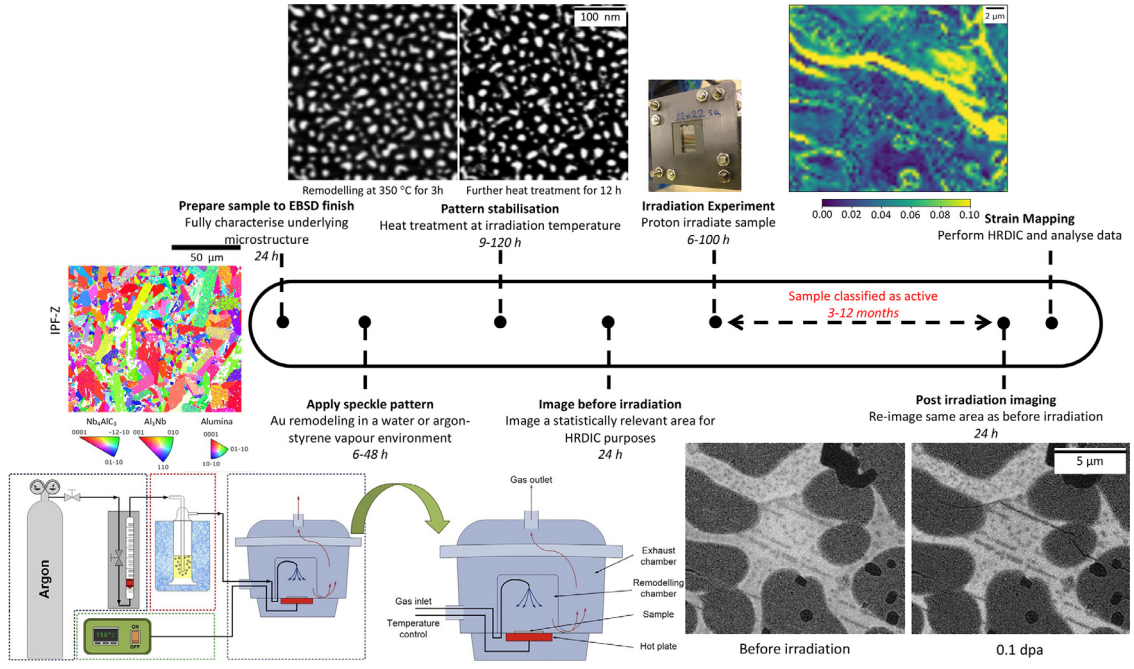

Fig. 2. Timeline of the experimental process, highlighting the importance of the irradiation experiment, as this is typically followed by a period of 3–12 months, during which 'active' samples are allowed to cool down. Styrene remodelling schematic from [29].

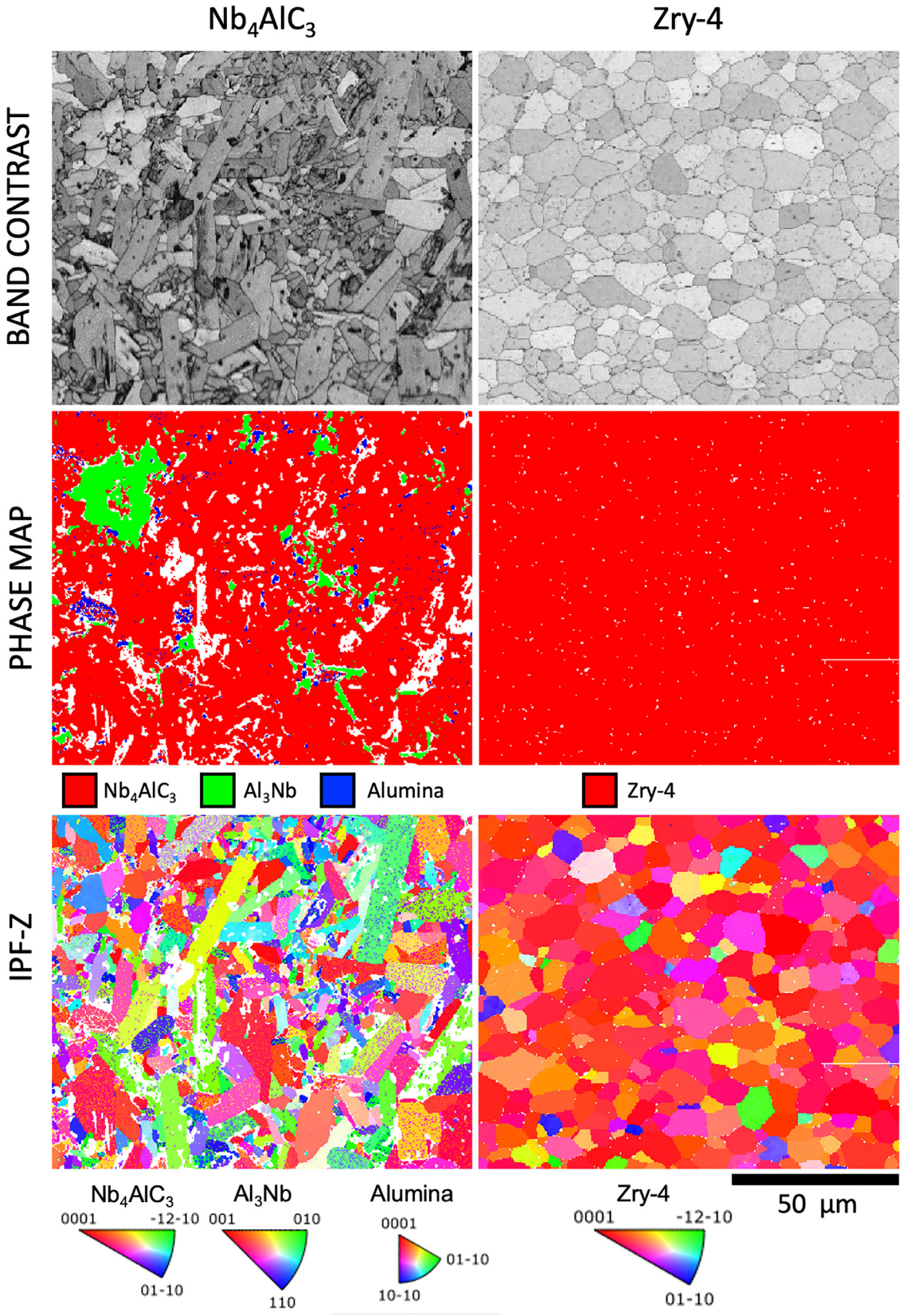

Fig. 3. Band contrast, phase, and grain orientation maps for Nb_4AlC_3 and Zry-4.

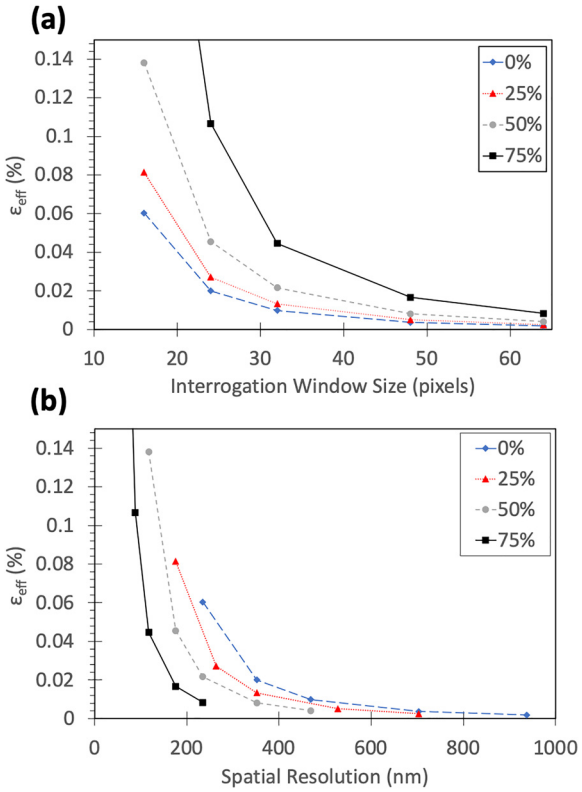

Fig. 4. Determination of HRDIC analysis parameters for one of the Zry-4 samples. Two sets of images taken before proton irradiation were correlated for different 'interrogation window' sizes and overlaps, and then the average systematic error was plotted as a function of (a) the 'interrogation window' size, and (b) the actual spatial resolution.

the pattern on $(Ta,Ti)_3AlC_2$ was further annealed in argon (Ar) atmosphere at 600 °C for 9 h, i.e., 50 °C below the irradiation temperature. A summary of the patterning conditions in terms of time and temperature for each sample is provided in Table 1.

2.3.2. Sample imaging & HRDIC processing

The gold pattern was imaged twice before and once after proton irradiation in the same area, using a FEI Magellan FEG-SEM (accelerating voltage: 5 kV, beam current: 0.8 nA, working distance: 4 mm) equipped with a concentric backscattered electron (CBS) detector. Assessment of the inherent noise in the pattern was achieved by taking the samples out of the microscope and reinserting them. The two images before irradiation were used to assess the inherent noise in the pattern. Images were taken at field widths of 30 μm for Nb_4AlC_3 and 20 μm for Zry-4 at a resolution of 2048 × 1768 pixels and using a dwell time of 5 μs, thus capturing image matrices of total areas of about (200–300) × (200–300) μm^2. The image sets were stitched together prior to the HRDIC analysis, using the '*Grid/Collection* stitching' function with a linear blend applied between images in ImageJ version 1.52p [44]. The linear blend was applied as it was found to result in little to no distortion in the stitched boundary when compared to not applying a blend. HRDIC analysis was performed using LaVision's DaVis software version 8.4.0 [45]. Local displacements were calculated by applying a standard Fast Fourier Transform (FFT) cross-correlation relative to the original image. To assess the systematic error and determine the appropriate 'interrogation window' size that provides the best balance between noise and spatial resolution, the two sets of images taken before proton irradiation were correlated. This gives a measurement of the uncertainty in the strain measurement and assesses the suitability of this technique for detecting changes caused by irradiation-induced damage, as the strains were expected to be very small and near the limit of the technique. 'Interrogation window' sizes ranging between 16 × 16 pixels and 64 × 64 pixels were assessed, using overlaps of 0, 25, 50, and 75%. Fig. 2 summarises the timeline of the experimental process, providing the key aspects and approximate durations of each process. Importantly, the nature of such study imposes a delay in imaging after irradiation to allow the induced activation to dissipate. Therefore, noise assessment is essential in checking the suitability of the applied pattern, while significant care must also be taken during sample mounting to avoid damaging the pattern.

2.3.3. Strain components

For mechanical loading experiments, the HRDIC results are presented predominantly as maps of ε_{11} and ε_{22}, i.e., the two in-plane directions. Alternatively, the effective shear strain (ε_{eff}) can be used, as this considers all the components of the in-plane strain [23,46]; ε_{eff} is used in this work to assess the systematic error. This component can be calculated using Eq. (1), where ε_{11} is the strain in the *x*-direction, ε_{22} is the strain in the *y*-direction, and ε_{12} is the in-plane shear. The governing equation is:

$$\boldsymbol{\varepsilon}_{\mathbf{eff}} = \sqrt{\left(\frac{\boldsymbol{\varepsilon}_{11} - \boldsymbol{\varepsilon}_{22}}{2}\right)^2 - \boldsymbol{\varepsilon}_{12}^2} \quad (1)$$

To assess irradiation-induced microstructural changes in all three materials, the principal strains ($\varepsilon_{1,2}$) have also been employed in the strain mapping analysis, as they reflect the directionality of the local strains. The principal strains are calculated from Eq. (2).

$$\boldsymbol{\varepsilon}_{1,2} = \frac{\boldsymbol{\varepsilon}_{11} + \boldsymbol{\varepsilon}_{22}}{2} \pm \sqrt{\left(\frac{\boldsymbol{\varepsilon}_{11} - \boldsymbol{\varepsilon}_{22}}{2}\right)^2 - \boldsymbol{\varepsilon}_{12}^2} \quad (2)$$

The detailed strain analysis was performed by exporting the in-plane displacement vector fields from DaVis and importing them into the DefDAP 0.93 Python package [47].

3. Suitability of proposed technique for determining irradiation induced strains

3.1. Materials characterisation

As irradiation effects were expected to correlate strongly with the local microstructure, grain orientation mapping was carried out by EBSD on both Nb_4AlC_3 and Zry-4 samples (Fig. 3); these maps were compared with strain maps, using DefDAP [47], acquired after proton irradiation to further the understanding of differences in strain localisation. The phase, band contrast (a measure of the EBSD pattern quality that facilitates the observation of grain boundaries), and IPF-*z* maps revealed that the Nb_4AlC_3 ceramic comprised a MAX phase volume fraction of 93%, excluding unindexed points, and its microstructure was characterised by MAX phase laths with an average length of 5.2 μm and an average width of 2.6 μm. The Zry-4 sample had an average grain size of 9.0 μm. This material showed also a strong preferential 'split-basal' texture, where basal poles were preferentially oriented in the normal direction (ND) with a spread of ±28° in the transverse direction (TD) [42]. The present study was conducted on the rolling direction-transverse direction (RD-TD) plane, which is the plane perpendicular to the proton beam. The distinct microstructural differences between these two materials in terms of grain shape & size, texture, porosity, and phase assembly could be linked to the strain maps, highlighting their effect on the response of these materials to proton irradiation.

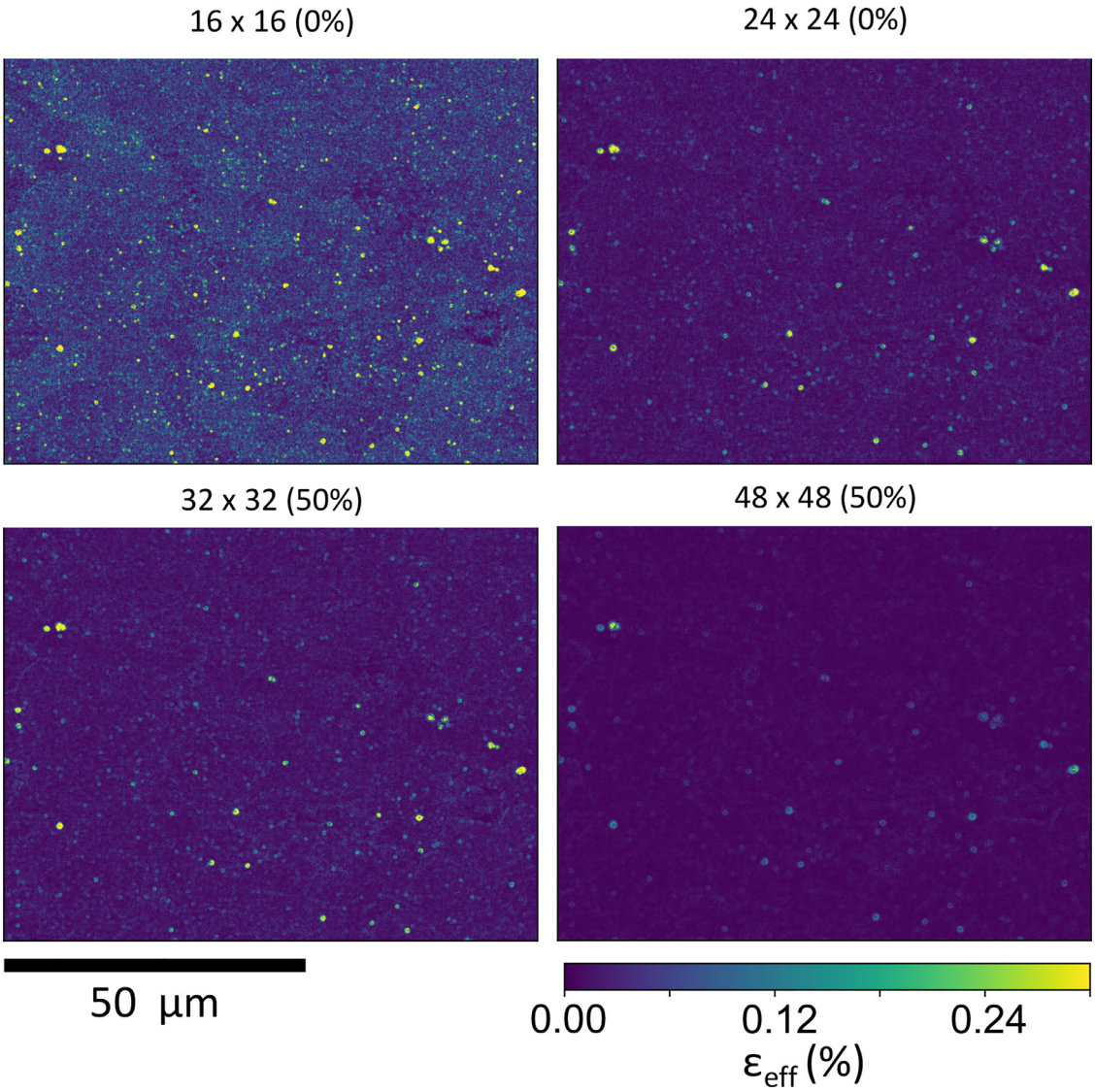

Fig. 5. Strain maps of systematic error using different HRDIC analysis parameters for one of the Zry-4 samples. Effective shear strain maps are shown for 16 × 16 pixels (0% overlap), 24 × 24 pixels (0% overlap), 32 × 32 pixels (50% overlap), and 48 × 48 pixels (50% overlap).

3.2. Irradiation-induced strain localisation: error assessment and material comparison

A crucial aspect of linking irradiation-induced strain localisation with the underlying material microstructure is to ensure that none of the material strain patterning features are an artefact of the selected HRDIC parameters. To demonstrate this, the systematic error for one of the Zry-4 samples has been initially compared in terms of the effective shear strain for different 'interrogation window' sizes and overlaps in Fig. 4, where two sets of images were collected before proton irradiation and correlated with each other. This allowed the optimum HRDIC parameters to be determined: Fig. 4a shows the noise measurements as a function of the 'interrogation window' size, and Fig. 4b converts this to the spatial resolution of the strain measurement. The measurements are considered as noise assessments, because they determine the changes in strain due to the image capture process. These results show quantitatively that as the 'interrogation window' size increases and the overlap decreases, the error in the average effective shear strain, ε_{eff}, decreases exponentially. However, the benefit of using a smaller 'interrogation window' is that the measurement spatial resolution increases, i.e., it becomes more likely to detect the true strain localisation associated with irradiation-induced effects, while the advantage of using a greater overlap is that it maximises the accuracy of the measurements. This can be observed from the strain maps in Fig. 5, where different correlation parameters are compared. Finer 'interrogation window' sizes and smaller overlaps lead to high-strain points and poor correlation in certain locations, whereas these features almost disappear with larger 'interrogation window' sizes and greater overlaps, thus improving the accuracy. In this study, the optimal balance between maximising spatial resolution and reducing noise was found using a 48 × 48 pixel 'interrogation window' size with a 50% overlap, as this gives a good trade-off between high spatial resolution and low noise.

3.2.1. Irradiation-induced material growth

The suitability of HRDIC for detecting irradiation-induced damage has been highlighted by presenting each strain component (i.e., the effective shear strain, ε_{eff}, and the local in-plane strains, ε_{11} & ε_{22}) for Zry-4 at 1 & 2 dpa and for the Nb_4AlC_3 MAX phase ceramic at ~0.1 dpa (Fig. 6). There is a marked difference in the mag-

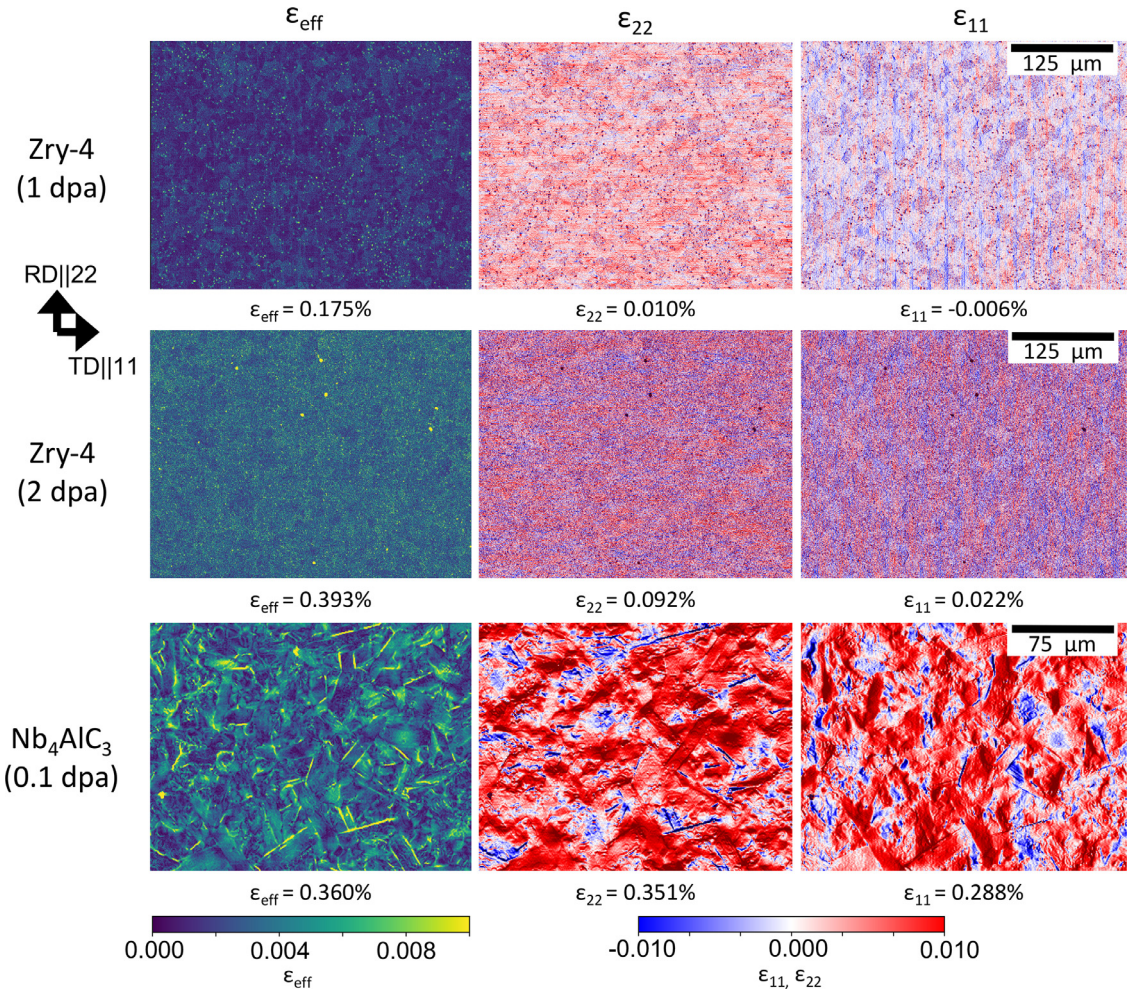

Fig. 6. Comparison of irradiation-induced strain localisation in Zry-4 (1 & 2 dpa) and Nb_4AlC_3 (-0.1 dpa) samples proton-irradiated at 350 °C in terms of the strain components ε_{eff}, ε_{11} and ε_{22}. The average strain values are also provided inside each strain map.

nitude of the response of these two materials to irradiation, with much clearer changes in strain for the Nb_4AlC_3 MAX phase particularly sharp lines of strain. However, despite the strain patterning in Zry-4 being less pronounced, there are still clear grain to grain variations in strain at both damage levels suggesting microstructural influence on the irradiation response is being detected. For the Zry-4, the average strain increases as the dose increases from 1 to 2 dpa, with greater expansion observed in the ε_{22} component (parallel to RD) and very little expansion in the ε_{11} component (parallel to TD). The expansion along RD is expected due to the underlying material texture and is aligned with the typical growth direction in this metallic alloy [2,3]. By contrast, the Nb_4AlC_3 MAX phase ceramic undergoes more extreme changes at the much lower damage level of ~0.1 dpa, with intense strain localisation along grain boundaries, as well as high & low strains in neighbouring grains, suggesting an orientation dependence of the degree of expansion within each grain, as expected based on the susceptibility of the MAX phases to anisotropic radiation swelling. It was also possible to observe strain gradients within specific grains in the Nb_4AlC_3 MAX phase sample, highlighting the capability of this analytical technique to not only depict grain-to-grain strain fluctuations but also intragranular strain gradients.

3.2.2. Irradiation-induced microcracking

The images acquired before and after irradiation cannot only be used for high-resolution strain mapping, but they also enable the visual inspection of regions that underwent obvious changes under irradiation. For Nb_4AlC_3, where significant strain localisation was detected, focussing on a specific region that showed no visible cracks prior to proton irradiation (Fig. 7a) revealed microcracking after irradiation (Fig. 7b). The post-irradiation image of this area shows three distinct cracks that have either propagated from one location or coalesced to provide a single crack longer than 20 μm (Fig. 7b). Furthermore, the effective shear & principal strain maps (Fig. 7c-e) of the same sample highlight the extent of localised microcracking in Nb_4AlC_3, where the displacement vectors (Fig. 7f) show the cracks opening. Since HRDIC analysis can be performed across many grains, the potential benefits of this analytical technique to study irradiation-induced damage are obvious, e.g., in identifying whether locations of microcracking are everywhere or correlate to particular phases or texture; these are observations that may be missed when focussing on single grains.

3.2.3. Speckle pattern quality requirements

Pattern stabilization. Accurate strain mapping relies strongly on a pre-applied speckle pattern that remains stable throughout the experiment, i.e., it does not undergo changes unless they stem directly from the experiment, for example, due to strain caused by an externally applied load (e.g., tension) or, in this case, induced by proton irradiation. Therefore, speckle pattern development (i.e., the spontaneous change of the pattern) at the irradiation temperature would have a detrimental impact on the observed strain fields,

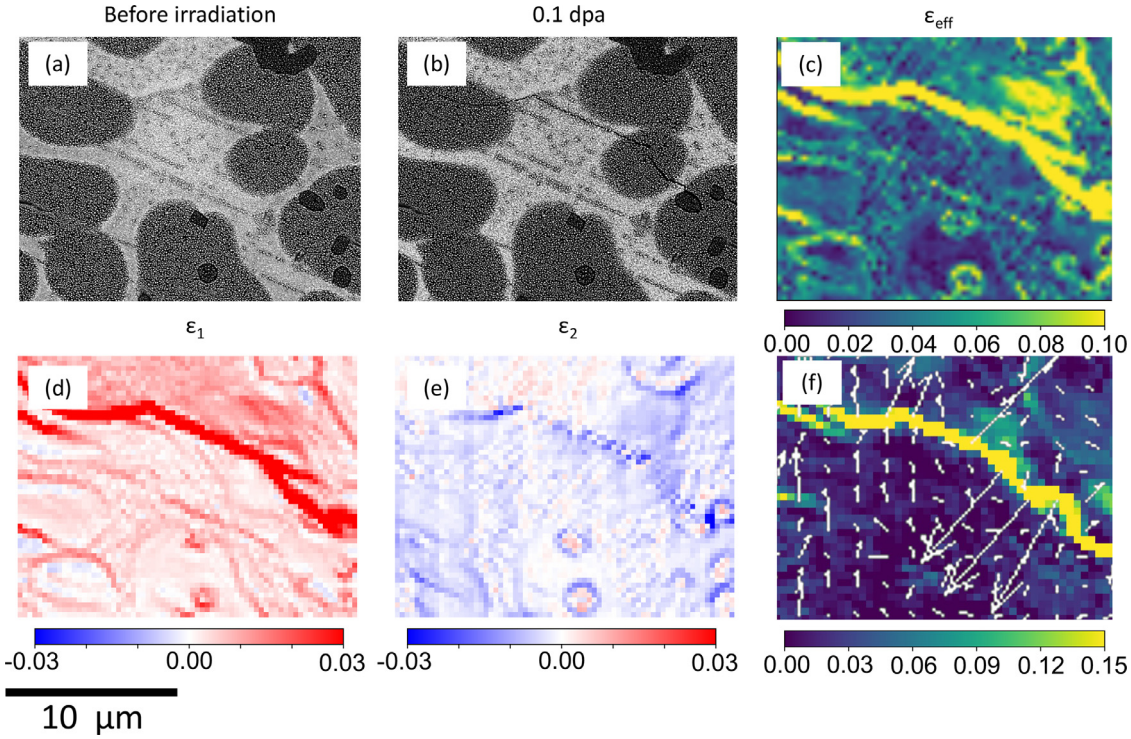

Fig. 7. Linking the underlying microstructure to strain localisation and microcracking in the Nb_4AlC_3 sample. CBS image of the Nb_4AlC_3 sample with a gold pattern applied (a) before and (b) after proton irradiation to ~0.1 dpa at 350 °C, and the comparative strain maps in terms of (c) ε_{eff}, (d) ε_1, (e) ε_2 and (f) ε_{eff} with the displacement vectors overlaid to show the cracking.

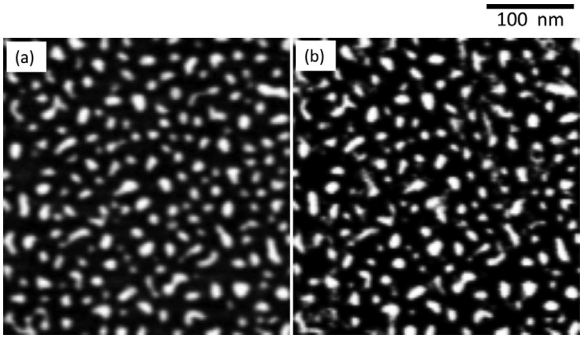

Fig. 8. Speckle pattern development with dwell time at 350 °C for one of the Zry-4 samples, after initial remodelling in a styrene environment at 200 °C for 36 h. Pattern after a dwell of (a) 3 h and (b) 12 h.

making it difficult to link the observed strains to the proton irradiation. For this reason, a pattern stabilisation heat treatment is performed at the irradiation temperature for ~4–5 times the normal remodelling time. Fig. 8 shows the evolution of the speckle pattern on a Zry-4 sample, after initial remodelling in a styrene environment at 200 °C for 36 h, upon annealing for 3 h & 12 h at the targeted irradiation temperature of 350 °C. After 3 h, the gold speckles appear relatively distinct and separated and would be suitable for use in deformation studies (Fig. 8a). However, Fig. 8b clearly demonstrates the requirement for a speckle pattern stabilisation heat treatment at the irradiation temperature, as further speckle ripening has occurred, and the individual speckles appear sharper. For the proton irradiation experiment itself, the pattern was heated for ~100 h. It should be noted that annealing at 350 °C does not affect the underlying microstructure of Zry-4 and this annealing time is similar to the time required for irradiations to higher dpa levels.

Pattern development during proton irradiation. The consequences of not having stabilised the speckle pattern prior to proton irradiation were investigated by choosing a pattern stabilisation temperature 50 °C below the targeted proton irradiation temperature. This was performed on the novel, multiphase $(Ta,Ti)_3AlC_2$ MAX phase-based ceramic, as pattern differences were likely to be more pronounced in such a sample, where individual phases would remodel differently, requiring different remodelling times. Fig. 9 shows the underlying material microstructure in comparison to the resulting strain maps after irradiation to enable the effects of the irradiation and remodelling temperatures to be assessed in parallel. It is apparent from the CBS images before (Fig. 9a) and after (Fig. 9b) irradiation that regions within the initially brighter $(Ta,Ti)_3AlC_2$ MAX phase grains have darkened after irradiation, indicating local changes in the microstructure; however, these changes cannot be determined from the raw unprocessed images. The strain maps (Fig. 9d-e) clearly show that there are regions exhibiting similar features to those observed in the Nb_4AlC_3 sample, with high strains near/at grain boundaries, previously linked to microcracking. When compared to Nb_4AlC_3, the number of potential cracks in the $(Ta,Ti)_3AlC_2$ ceramic is considerably higher and this is attributed to its lower MAX phase content in combination with a high volume fraction of mixed $(Ta,Ti)C_x$ carbide phases. Very little strain localisation is observed in the pseudo-binary carbide grains themselves, however, the expected incompatibility at most grain boundaries due to the irradiation growth of the $(Ta,Ti)_3AlC_2$ MAX phase grains leads to the observed material microcracking.

In the same sample, the expansion of the grains of the novel $(Ta,Ti)_3AlC_2$ MAX phase solid solution resulted in a very homogeneous strain distribution, which typically occurs when the speckle pattern has either changed or has been removed. Further comparison of high-magnification CBS images of a $(Ta,Ti)_3AlC_2$ MAX phase grain and a $(Ta,Ti)C_x$ pseudo-binary carbide grain before and after

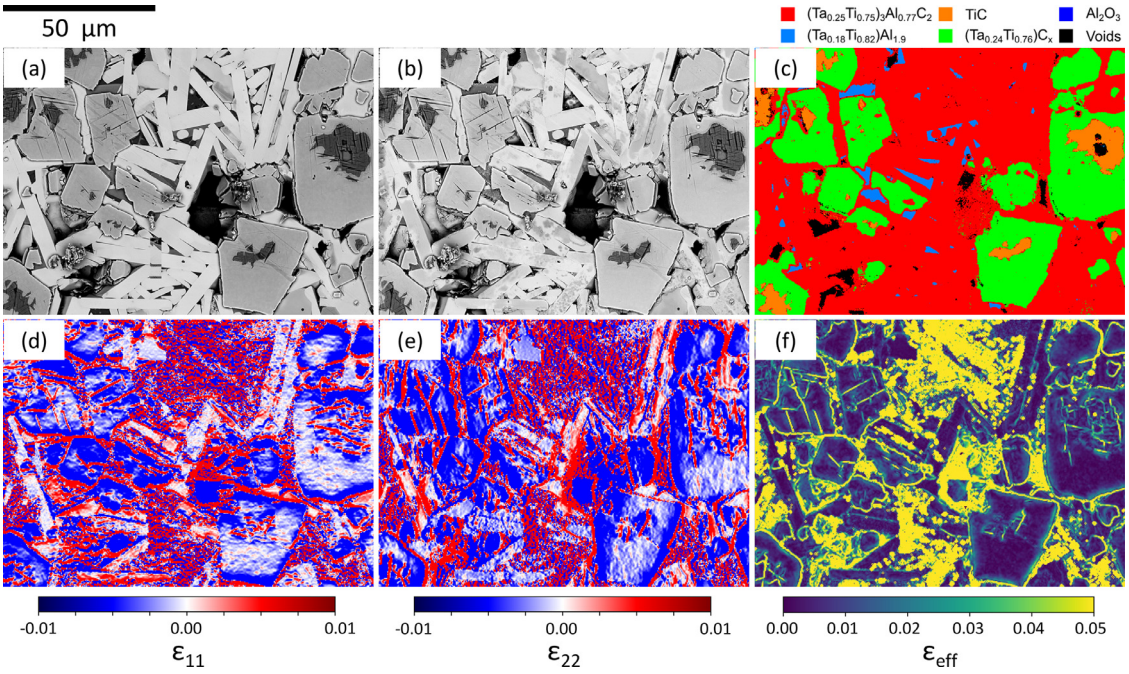

Fig. 9. Influence of remodelling at a lower temperature than the irradiation temperature on the observed strain maps for the $(Ta,Ti)_3AlC_2$ MAX phase-based ceramic that was proton irradiated to ~0.1 dpa (0.11 dpa) at 650 °C. CBS images of the underlying microstructure with the speckle pattern applied (a) before and (b) after proton irradiation with (c) the accompanying phase map captured from energy-dispersive X-ray spectroscopy (EDS) in comparison to the (d) ε_{11}, (e) ε_{22} and (f) ε_{eff} strain maps.

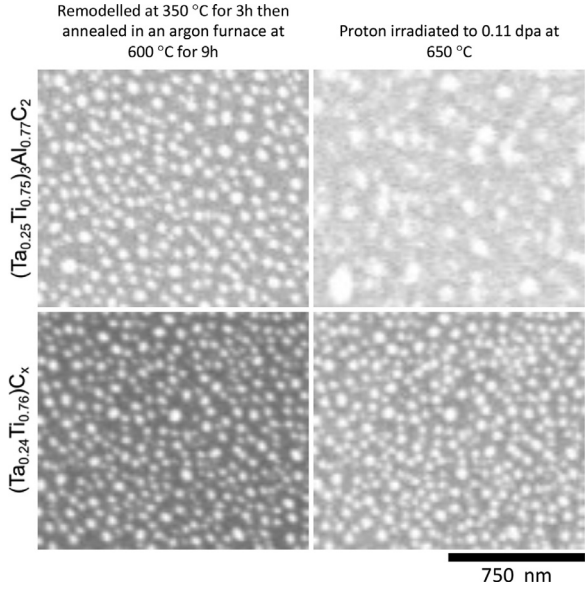

Fig. 10. Speckle pattern development during the proton irradiation of a $(Ta,Ti)_3AlC_2$ MAX phase grain at 650 °C to 0.11 dpa, as compared to a $(Ti,Ta)C_x$ carbide grain with the $(Ta_{0.24},Ti_{0.76})_3C_x$ stoichiometry.

proton irradiation clearly shows a significant speckle pattern evolution in the MAX phase grain as opposed to the pseudo-binary carbide grain (Fig. 10). Therefore, only the effects observed in the pseudo-binary carbide grains can be considered to result from proton irradiation, while the effects in the MAX phase grains are associated with the temperature, confirming that the speckle pattern must be stabilised at the irradiation temperature. Additional experiments must be conducted in the future on other phase-impure MAX phase ceramics with stabilised speckle patterns to confirm the previous hypothesis. The more severe speckle pattern development in the MAX phase grains as compared to the pseudo-binary carbide grains could be attributed to the greater anisotropy of the MAX phase crystal structure; the latter is reflected in the MAX phase-specific response to both heating (i.e., anisotropic thermal expansion) and irradiation (i.e., anisotropic radiation-induced swelling).

3.2.4. Perspective uses of the methodology

Small-scale mechanical testing of irradiated materials is gaining popularity in assessing irradiation-induced changes in the mechanical properties of nuclear materials [48], as small material volumes can currently be used to extract quantitative information on the material response to irradiation damage, provided that test standards specifically designed and adapted to the needs of miniaturised samples have been developed. The methodology proposed here is a valuable tool that could be included in the overall small-scale testing strategy to directly evaluate the impact of microstructural and compositional changes on the radiation tolerance of new materials. Furthermore, if (scoping) ion/proton irradiation is combined with in-situ thermomechanical loading, the material response to reactor-relevant operation conditions (temperature, irradiation, stress) could be confidently assessed and the determined by such synergistic testing key material parameters (e.g., yield stress, creep rate, etc.) can eventually be included within plasticity modelling for lifetime predictions.

4. Conclusions

This work demonstrated the ability of HRDIC to measure strain localisation on a microstructural level as result of proton irradiation, providing a new analytical tool that can be used to assess the irradiation-induced damage evolution in different nuclear materials (metals & ceramics). Gold remodelled patterns proved, for the most part, resilient to proton irradiation for doses ranging between ~0.1 dpa and 2 dpa, and moderate irradiation temperatures (i.e., 350–650 °C). Comparing the strain localisation in three different materials with significant expected differences in radiation response provided clear evidence of strong strain localisation in

Nb_4AlC_3 and $(Ta,Ti)_3AlC_2$ MAX phase-based ceramics irradiated to ~0.1 dpa. In both MAX phase ceramics, strong strain localisation was considered the cause of the observed microcracking in specific sample areas. On the other hand, Zry-4 samples irradiated to 1 & 2 dpa exhibited grain-to-grain variations but much less strain localisation at grain boundaries, with a clearly observed difference in irradiation growth (expansion) between the rolling and transverse directions.

The stability of the speckle pattern during proton irradiation paves the way towards the systematic use of this technique to complement irradiation creep studies with ex-situ strain localisation measurements to understand the deformation mechanisms at the nanoscale.

Declaration of Competing Interest

The authors declare that they have no known competing financial interests or personal relationships that could have appeared to influence the work reported in this paper.

CRediT authorship contribution statement

D. Lunt: Conceptualization, Methodology, Formal analysis, Investigation, Writing – original draft, Writing – review & editing, Visualization. **R. Thomas:** Formal analysis, Writing – review & editing, Visualization. **D. Bowden:** Methodology, Investigation, Writing – review & editing. **M.T.P. Rigby-Bell:** Resources, Investigation, Writing – review & editing. **S. de Moraes Shubeita:** Investigation, Writing – review & editing. **C. Andrews:** Investigation, Writing – review & editing. **T. Lapauw:** Resources, Writing – review & editing. **J. Vleugels:** Resources, Writing – review & editing. **J. Quinta da Fonseca:** Writing – review & editing, Visualization, Methodology. **K. Lambrinou:** Writing – review & editing, Visualization, Supervision, Project administration, Funding acquisition. **P. Frankel:** Conceptualization, Writing – review & editing, Visualization, Supervision, Project administration, Funding acquisition.

Data availability

The images and data used in this study can be readily accessed by contacting the corresponding author.

Acknowledgments

This research has been funded by the Euratom research and training program 2014–2018 under Grant Agreement No. 740415 (H2020 IL TROVATORE). The performed research falls within the framework of the European Energy Research Alliance (EERA) Joint Programme on Nuclear Materials (JPNM). This work was also supported through the Carbides for Future Fission Environments (CaFFE) project grant number EP/M018482/1 and MIDAS (Mechanistic understanding of Irradiation Damage in fuel Assemblies) programme grant (EP/S01702X/1). David Lunt would like to acknowledge funding through EPSRC Fusion Grant EP/W006839/1. Professor João Quinta da Fonseca acknowledges funding through the LightForm EPSRC programme grant (EP/R001715/1). The microscopy was carried out at the University of Manchester Electron Microscopy Centre and all authors would like to thank the technical support staff.

References

[1] L. Hallstadius, S. Johnson, E. Lahoda, Cladding for high performance fuel, Prog. Nucl. Energy 57 (2012) 71–76, doi:10.1016/j.pnucene.2011.10.008.
[2] S. Yagnik, R.B. Adamson, G. Kobylyansky, J.H. Chen, D. Gilbon, S. Ishimoto, T. Fukuda, L. Hallstadius, A. Obukhov, S. Mahmood, Effect of alloying elements, cold work, and hydrogen on the irradiation-induced growth behavior of zirconium alloy variants, ASTM Spec. Tech. Publ. STP 1597 (2018) 748–795, doi:10.1520/STP159720160040.
[3] K. Kakiuchi, M. Amaya, Y. Udagawa, Irradiation growth behavior and effect of hydrogen absorption of Zr-based cladding alloys for PWR, Ann. Nucl. Energy 171 (2022) 109004, doi:10.1016/j.anucene.2022.109004.
[4] E.N. Hoffman, D.W. Vinson, R.L. Sindelar, D.J. Tallman, G. Kohse, M.W. Barsoum, MAX phase carbides and nitrides: properties for future nuclear power plant in-core applications and neutron transmutation analysis, Nucl. Eng. Des. 244 (2012) 17–24, doi:10.1016/j.nucengdes.2011.12.009.
[5] Z.M. Sun, Progress in research and development on MAX phases: a family of layered ternary compounds, Int. Mater. Rev. 56 (2011) 143–166, doi:10.1179/1743280410Y.0000000001.
[6] C. Ang, C. Silva, C. Shih, T. Koyanagi, Y. Katoh, S.J. Zinkle, Anisotropic swelling and microcracking of neutron irradiated Ti_3AlC_2-$Ti_5Al_2C_3$ materials, Scr. Mater. 114 (2016) 74–78, doi:10.1016/j.scriptamat.2015.11.008.
[7] D.J. Tallman, L. He, J. Gan, E.N. Caspi, E.N. Hoffman, M.W. Barsoum, Effects of neutron irradiation of Ti_3SiC_2 and Ti_3AlC_2 in the 121–1085 °C temperature range, J. Nucl. Mater. 484 (2017) 120–134, doi:10.1016/j.jnucmat.2016.11.016.
[8] J. Ward, S. Middleburgh, M. Topping, A. Garner, D. Stewart, M.W. Barsoum, M. Preuss, P. Frankel, Crystallographic evolution of MAX phases in proton irradiating environments, J. Nucl. Mater. 502 (2018) 220–227, doi:10.1016/j.jnucmat.2018.02.008.
[9] H.H. Qarra, K.M. Knowles, M.E. Vickers, S. Akhmadaliev, K. Lambrinou, Heavy ion irradiation damage in Zr_2AlC MAX phase, J. Nucl. Mater. 523 (2019) 1–9, doi:10.1016/j.jnucmat.2019.05.034.
[10] B. Tunca, G. Greaves, J.A. Hinks, P.O.Å. Persson, J. Vleugels, K. Lambrinou, In situ He+ irradiation of the double solid solution $(Ti_{0.5},Zr_{0.5})_2(Al_{0.5},Sn_{0.5})C$ MAX phase: defect evolution in the 350–800 °C temperature range, Acta Mater. 206 (2021) 116606, doi:10.1016/j.actamat.2020.116606.
[11] J. Ward, D. Bowden, E. Prestat, S. Holdsworth, D. Stewart, M.W. Barsoum, M. Preuss, P. Frankel, Corrosion performance of Ti_3SiC_2, Ti_3AlC_2, Ti_2AlC and Cr_2AlC MAX phases in simulated primary water conditions, Corros. Sci. (2018), doi:10.1016/j.corsci.2018.04.034.
[12] V.D. Jovic, B.M. Jovic, S. Gupta, T. El-Raghy, M.W. Barsoum, Corrosion behavior of select MAX phases in NaOH, HCl and H_2SO_4, Corros. Sci. 48 (2006) 4274–4282, doi:10.1016/j.corsci.2006.04.005.
[13] T. Lapauw, B. Tunca, J. Joris, A. Jianu, R. Fetzer, A. Weisenburger, J. Vleugels, K. Lambrinou, Interaction of $M_{n+1}AX_n$ phases with oxygen-poor, static and fast-flowing liquid lead-bismuth eutectic, J. Nucl. Mater. 520 (2019) 258–272, doi:10.1016/j.jnucmat.2019.04.010.
[14] B. Tunca, T. Lapauw, C. Callaert, J. Hadermann, R. Delville, E.N. Caspi, M. Dahlqvist, J. Rosén, A. Marshal, K.G. Pradeep, J.M. Schneider, J. Vleugels, K. Lambrinou, Compatibility of Zr_2AlC MAX phase-based ceramics with oxygen-poor, static liquid lead–bismuth eutectic, Corros. Sci. 171 (2020) 108704, doi:10.1016/j.corsci.2020.108704.
[15] D. Bowden, J. Ward, S. Middleburgh, S. de Moraes Shubeita, E. Zapata-Solvas, T. Lapauw, J. Vleugels, K. Lambrinou, W.E. Lee, M. Preuss, P. Frankel, The stability of irradiation-induced defects in Zr_3AlC_2, Nb_4AlC_3 and $(Zr_{0.5},Ti_{0.5})_3AlC_2$ MAX phase-based ceramics, Acta Mater. 183 (2020) 24–35, doi:10.1016/j.actamat.2019.10.049.
[16] F. Hild, S. Roux, Digital image correlation: from displacement measurement to identification of elastic properties - a review, Strain. 42 (2006) 69–80.
[17] F. Hild, S. Roux, Comparison of local and global approaches to digital image correlation, Exp. Mech. (2012) 1503–1519, doi:10.1007/s11340-012-9603-7.
[18] M.A. Sutton, F. Hild, Recent advances and perspectives in digital image correlation, Exp. Mech. (2015) 1–8, doi:10.1007/s11340-015-9991-6.
[19] D. Lunt, R. Thomas, M. Roy, J. Duff, M. Atkinson, P. Frankel, M. Preuss, J. Quinta da Fonseca, Comparison of sub-grain scale digital image correlation calculated using commercial and open-source software packages, Mater. Charact. 163 (2020) 110271, doi:10.1016/j.matchar.2020.110271.
[20] A. Harte, M. Atkinson, A. Smith, C. Drouven, S. Zaefferer, J.Q. da Fonseca, M. Preuss, The effect of solid solution and gamma prime on the deformation modes in Ni-based superalloys, Acta Mater. (2020), doi:10.1016/j.actamat.2020.04.004.
[21] D. Lunt, A. Ho, A. Davis, A. Harte, F. Martina, J. Quinta da Fonseca, P. Prangnell, The effect of loading direction on strain localisation in wire arc additively manufactured Ti–6Al–4V, Mater. Sci. Eng. A 788 (2020) 139608, doi:10.1016/j.msea.2020.139608.
[22] A.W. Mello, T.A. Book, A. Nicolas, S.E. Otto, C.J. Gilpin, M.D. Sangid, Distortion correction protocol for digital image correlation after scanning electron microscopy: emphasis on long duration and *ex-situ* experiments, Exp. Mech. (2017) 1–15, doi:10.1007/s11340-017-0303-1.
[23] F. Gioacchino, J. Quinta da Fonseca, Plastic strain mapping with sub-micron resolution using digital image correlation, Exp. Mech. (2012), doi:10.1007/s11340-012-9685-2.
[24] J.P.M. Hoefnagels, M.P.F.H.L. van Maris, T. Vermeij, One-step deposition of nano-to-micron-scalable, high-quality digital image correlation patterns for high-strain *in-situ* multi-microscopy testing, Strain. 55 (2019) 1–13, doi:10.1111/str.12330.
[25] T. Vermeij, J.P.M. Hoefnagels, Plasticity, localization, and damage in ferritic-pearlitic steel studied by nanoscale digital image correlation, Scr. Mater. 208 (2022) 114327, doi:10.1016/j.scriptamat.2021.114327.
[26] J.D. Carroll, W. Abuzaid, J. Lambros, H. Sehitoglu, High resolution digital image correlation measurements of strain accumulation in fatigue crack growth, Int. J. Fatigue. (2012), doi:10.1016/j.ijfatigue.2012.06.010.
[27] D. Lunt, A. Orozco-Caballero, R. Thomas, P. Honniball, P. Frankel, M. Preuss, J. Quinta da Fonseca, J. Quinta, R. Thomas, P. Honniball, P. Frankel, M. Preuss,

Enabling high resolution strain mapping in zirconium alloys, Mater. Charact. 139 (2018) 355–363, doi:10.1016/j.matchar.2018.03.014.
[28] D. Lunt, T. Busolo, X. Xu, J. Quinta da Fonseca, M. Preuss, Effect of nanoscale α_2 precipitation on strain localisation in a two-phase Ti-alloy, Acta Mater. 129 (2017) 72–82, doi:10.1016/j.actamat.2017.02.068.
[29] A. Orozco-Caballero, D. Lunt, J.D.J.D. Robson, J. Quinta da Fonseca, How magnesium accommodates local deformation incompatibility : a high-resolution digital image correlation study, Acta Mater. 133 (2017) 367–379, doi:10.1016/j.actamat.2017.05.040.
[30] M.T.P. Rigby, V. Natu, M. Sokol, D.J. Kelly, D.G. Hopkinson, Y. Zou, J.R.T. Bird, L.J. Evitts, M. Smith, C.P. Race, P. Frankel, S.J. Haigh, M.W. Barsoum, Synthesis of new M-layer solid-solution 312 MAX phases $(Ta_{1-x}Ti_x)_3AlC_2$ (x = 0.4, 0.62, 0.75, 0.91 or 0.95), and their corresponding MXenes, RSC Adv. 11 (2021) 3110–3114, doi:10.1039/d0ra09761f.
[31] M.D. McMurtrey, B. Cui, I. Robertson, D. Farkas, G.S. Was, Mechanism of dislocation channel-induced irradiation assisted stress corrosion crack initiation in austenitic stainless steel, Curr. Opin. Solid State Mater. Sci. 19 (2015) 305–314, doi:10.1016/j.cossms.2015.04.001.
[32] M.R. He, D.C. Johnson, G.S. Was, I.M. Robertson, The role of grain boundary microchemistry in irradiation-assisted stress corrosion cracking of a Fe-13Cr-15Ni alloy, Acta Mater. 138 (2017) 61–71, doi:10.1016/j.actamat.2017.07.042.
[33] R. Schäublin, A. Ramar, N. Baluc, V. de Castro, M.A. Monge, T. Leguey, N. Schmid, C. Bonjour, Microstructural development under irradiation in European ODS ferritic/martensitic steels, J. Nucl. Mater. 351 (2006) 247–260, doi:10.1016/j.jnucmat.2006.02.005.
[34] L. Tournadre, F. Onimus, J.L. Béchade, D. Gilbon, J.M. Cloué, J.P. Mardon, X. Feaugas, Toward a better understanding of the hydrogen impact on the radiation induced growth of zirconium alloys, J. Nucl. Mater. 441 (2013) 222–231, doi:10.1016/j.jnucmat.2013.05.045.
[35] A. Harte, M. Topping, P. Frankel, D. Jädernäs, J. Romero, L. Hallstadius, E.C. Darby, M. Preuss, Nano-scale chemical evolution in a proton-and neutron-irradiated Zr alloy, J. Nucl. Mater. 487 (2017) 30–42, doi:10.1016/j.jnucmat.2017.01.049.
[36] A. Harte, D. Jädernäs, M. Topping, P. Frankel, C.P. Race, J. Romero, L. Hallstadius, E.C. Darby, M. Preuss, The effect of matrix chemistry on dislocation evolution in an irradiated Zr alloy, Acta Mater. 130 (2017) 69–82, doi:10.1016/j.actamat.2017.03.024.
[37] A. Sarkar, A. Kumar, S. Mukherjee, S.K. Sharma, D. Dutta, P.K. Pujari, A. Agarwal, S.K. Gupta, P. Singh, J.K. Chakravartty, Investigation of microstructure and mechanical properties of proton irradiated Zircaloy 2, J. Nucl. Mater. 479 (2016) 524–532, doi:10.1016/j.jnucmat.2016.07.050.
[38] D.W. Clark, S.J. Zinkle, M.K. Patel, C.M. Parish, High temperature ion irradiation effects in MAX phase ceramics, Acta Mater. 105 (2016) 130–146, doi:10.1016/j.actamat.2015.11.055.
[39] J. Ward, D. Bowden, D. Stewart, M.W. Barsoum, P. Frankel, M. Preuss, Influence of proton-irradiation temperature on the damage accumulation in Ti_3SiC_2 and Ti_3AlC_2, Scr. Mater. 165 (2019) 98–102, doi:10.1016/j.scriptamat.2019.02.022.
[40] N.T.H. Trung, H.S.M. Phuong, M.D. Starostenkov, V.V. Romanenko, V.A. Popov, Threshold displacement energy in Ni, Al and B_2NiAl, IOP Conf. Ser. Mater. Sci. Eng. (2018) 447, doi:10.1088/1757-899X/447/1/012004.
[41] F. Di Gioacchino, J.Quinta Da Fonseca, An experimental study of the polycrystalline plasticity of austenitic stainless steel, Int. J. Plast. 74 (2015) 92–109, doi:10.1016/j.ijplas.2015.05.012.
[42] R. Thomas, D. Lunt, M.D. Atkinson, J. Quinta da Fonseca, M. Preuss, F. Barton, J. O'Hanlon, P. Frankel, Characterisation of irradiation enhanced strain localisation in a zirconium alloy, Materialia 5 (2019) 100248, doi:10.1016/j.mtla.2019.100248.
[43] C. Dichtl, D. Lunt, M. Atkinson, R. Thomas, A. Plowman, B. Barzdajn, R. Sandala, J.Q. da Fonseca, M. Preuss, Slip activity during low-stress cold creep deformation in a near-α titanium alloy, Acta Mater. (2022) 117691, doi:10.1016/j.actamat.2022.117691.
[44] J. Schindelin, I. Arganda-Carreras, E. Frise, V. Kaynig, M. Longair, T. Pietzsch, S. Preibisch, C. Rueden, S. Saalfeld, B. Schmid, J.Y. Tinevez, D.J. White, V. Hartenstein, K. Eliceiri, P. Tomancak, A. Cardona, Fiji: an open-source platform for biological-image analysis, Nat. Methods 9 (2012) 676–682, doi:10.1038/nmeth.2019.
[45] LaVision DaVis version 8.4.0 digital image correlation software.
[46] H.A. Padilla, J. Lambros, A.J. Beaudoin, I.M. Robertson, Relating inhomogeneous deformation to local texture in zirconium through grain-scale digital image correlation strain mapping experiments, Int. J. Solids Struct. 49 (2012) 18–31, doi:10.1016/j.ijsolstr.2011.09.001.
[47] M.D. Atkinson, R. Thomas, A. Harte, P. Crowther, J. Quinta da Fonseca, DefDAP: deformation data analysis in python, (2020). 10.5281/zenodo.3688097.
[48] P. Hosemann, Small-scale mechanical testing on nuclear materials: bridging the experimental length-scale gap, Scr. Mater. 143 (2018) 161–168, doi:10.1016/j.scriptamat.2017.04.026.